# Measurement of the $^{141}$Pr$(n, \gamma)$ cross section up to stellar *s*-process temperatures at the China Spallation Neutron Source Back-n facility

Xiankai Li,[1,2] Zhendong An,[2,3,4,5,*] Wei Jiang,[6,7] Jingyi Zhang,[2] Ruoran Bai,[2] Shaokun Liu,[2] Xinxiang Li,[1,3,8,†] Zhichao Zhu,[1,‡] Gaole Yang,[2] Weiwei Qiu,[9,4,5] Zhengfa Liao,[9,4,5] Ziyue Zhuang,[9,4,5] Xiaoping Zhang,[4,5] Shengli Chen,[9] Chenchen Guo,[9] Erxi Xiao,[9] Xiao Fang,[9] Hongwei Wang,[3,8,10] Xinrong Hu,[3,8] Bing Jiang,[3,8] Wenqing Shen,[3,10] Jincheng Wang,[11] Jie Ren,[11] Xichao Ruan,[11] Wen Luo,[1] Haoyang Lan,[1,12,13] Zongwei Cao,[1] Xu Ma,[14,11] Yingdu Liu,[14] Pusen Wang,[14] Yi Yang,[15] Ping Su,[15] Xiangai Deng,[15] Wanbing He,[15] Yugang Ma,[15,3] Chunwang Ma,[16,17] Yuting Wang,[16,17] Zhitao Dai,[18] Ertao Li,[19] Pengqin He,[2] RenGuang Tang,[2] Tao Zhou,[2] Jing Wang,[2] Han Yi,[6,7] Yue Zhang,[6,7] Yonghao Chen,[6,7] Ruirui Fan,[6,7] Keqing Gao,[6,7] Qiang Li,[6,7] Kang Sun,[6,7] Zhixin Tan,[6,7] Minhao Gu,[6,7] Hantao Jing,[6,7] and Jingyu Tang[6,7]
(CSNS Back-n Collaboration)

[1]*School of Nuclear Science and Technology, University of South China, Hengyang 421001, China*
[2]*School of Physics and Astronomy, Sun Yat-sen University, Zhuhai 519082, China*
[3]*Shanghai Institute of Applied Physics, Chinese Academy of Sciences, Shanghai 201800, China*
[4]*State Key Laboratory of Lunar and Planetary Sciences, Macau University of Science and Technology, Macau 999078, China*
[5]*CNSA Macau Center for Space Exploration and Science, Macau 999078, China*
[6]*Institute of High Energy Physics, Chinese Academy of Sciences, Beijing 100049, China*
[7]*Spallation Neutron Source Science Center, Dongguan 523803, China*
[8]*University of Chinese Academy of Sciences, Beijing 100049, China*
[9]*Sino-French Institute of Nuclear Engineering and Technology, Sun Yat-sen University, Zhuhai 519082, China*
[10]*Shanghai Advanced Research Institute, Chinese Academy of Sciences, Shanghai 201210, China*
[11]*Key Laboratory of Nuclear Data,China Institute of Atomic Energy, Beijing 102413, China*
[12]*State Key Laboratory of Nuclear Physics and Technology and CAPT, Peking University, Beijing 100871, China*
[13]*Beijing Laser Acceleration Innovation Center, Huairou, Beijing 101400, China*
[14]*Shool of Materials Science and Engineering, Xiangtan University, Xiangtan 411100, China*
[15]*Key Laboratory of Nuclear Physics and Ion-beam Application (MOE), Institute of Modern Physics, Department of Nuclear Science and Technology, Fudan University, Shanghai 200433, China*
[16]*Institute of Particle and Nuclear Physics, Henan Normal University, Xinxiang 453007, China*
[17]*School of Physics, Henan Normal University, Xinxiang 453007, China*
[18]*Shenzhen Center, Cancer hospital, Chinese Academy of Medical Sciences, Shenzhen 518100, China*
[19]*Institute for Advanced Study in Nuclear Energy and Safety, College of Physics and Optoelectronic Engineering, Shenzhen University, Shenzhen 518060, China*

(Received 3 March 2023; revised 30 May 2023; accepted 28 July 2023; published 6 September 2023)

In nuclear astrophysics, $^{141}$Pr is mainly produced by an *s* process, which has a neutron magic number ($N = 82$) leading to its low capture cross section and strongly affecting the *s* process. Its neutron capture cross section is an important input parameter for nuclear astrophysical network calculations. According to the EXFOR database, the measurement precision for the $^{141}$Pr$(n, \gamma)$ cross section should be improved in the resolved and unresolved resonance region. The $(n, \gamma)$ cross section of $^{141}$Pr was measured between 1 eV and 500 keV at the Back-n facility of the Chinese Spallation Neutron Source using the time-of-flight (TOF) method. The prompt $\gamma$ rays were detected by four $C_6D_6$ liquid scintillator detectors, and the data was analyzed using the pulse-height weighting technique (PHWT). The majority of results are in agreement with the evaluated data libraries ENDF/B-VIII.0, JENDL-5.0, and TENDL-2021, with some significant exceptions for small resonances. The multilevel *R*-matrix Bayesian code SAMMY was used to extract the resonance parameters of $^{141}$Pr in the resolved resonance region. And the Maxwell average cross section (MACS) from $kT = 5$ to 100 keV is calculated in the temperature range of the *s*-process nucleosynthesis model. In particular, at $kT = 30$ keV the MACS value of $^{141}$Pr is $145.0 \pm 13.7$ mb, which shows an obvious discrepancy with the Karlsruhe Astrophysical Database of Nucleosynthesis in Stars (KADoNiS) recommended value $111.4 \pm 1.4$ mb.

DOI: 10.1103/PhysRevC.108.035802

*anzhendong@mail.sysu.edu.cn
†lixinxiang@usc.edu.cn
‡22770662@qq.com

 

## I. INTRODUCTION

Elements heavier than iron are mainly produced by neutron capture. The astrophysical origin of these nuclides comes from at least two neutron capture processes, the so-called *s* process [1] and the *r* process [2]. The *s* process usually occurs in stars with low neutron density, typically asymptotic giant branch stars. During the *s* process, the seed nucleus undergoes neutron capture to form isotopes with higher atomic mass. If the new isotope is stable, a series of mass increases occurs, but if it is unstable, $\beta$ decay occurs and the next element with a higher atomic number is produced. The relative abundances of the elements and isotopes produced depend on the source of the neutrons and how their flux changes over time [3]. The *r* process requires one or more heavy seeded nuclei to capture neutrons in rapid succession, and the nuclei do not have time to undergo radioactive decay (usually via $\beta$ decay). Therefore, it mainly occurs during supernova explosions or binary neutron-star mergers. Due to the extreme neutron density, the seed nucleus is always in the process of neutron capture, the sequence that can continue up to the limit of stability of the increasingly neutron-rich nuclei (the neutron drip line) [4].

The nuclide $^{141}$Pr has a neutron magic number ($N = 82$), resulting in a lower neutron capture cross section and placement on the main *s*-process path. The *s*-process evolution path near the $^{141}$Pr isotope are shown in Fig. 1. The stellar neutron capture cross section (MACS) are indispensable data for nuclear astrophysical network research. To obtain the data, experimental measurements of the neutron capture cross section must be conducted within an energy range of several hundred eV to several hundred keV, followed by convolution with the neutron energy distribution in the stellar plasma environment [5]. Therefore, continuous measurements of the neutron capture cross section of $^{141}$Pr through experiments, particularly in the keV energy region, are crucial. On the other hand, $^{141}$Pr is one of the isotopic products with a large fission yield in fast reactors, which makes it very easy to accumulate in the spent fuel [6]. Therefore, obtaining accurate neutron capture cross sections for $^{141}$Pr is also crucial for reactor safety assessment.

Figure 2 shows the previous measurements of $^{141}$Pr $(n, \gamma)$ cross sections. Yoon *et al.* [7] made measurements between

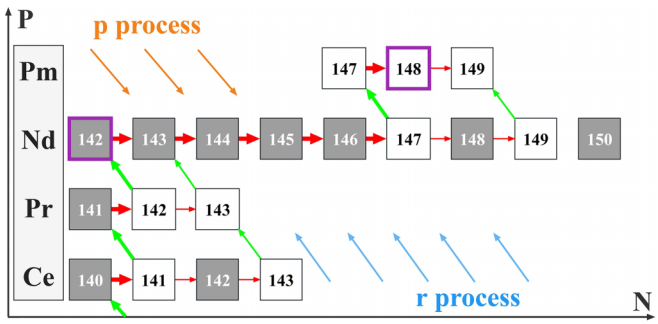


FIG. 1. Synthetic network diagram of nuclei near $^{141}$Pr isotopes. The gray boxes represent stable isotopes and the white boxes represent unstable isotopes. Boxes with purple borders represent *s*-only nuclei. The bold lines represent the main *s*-process path.

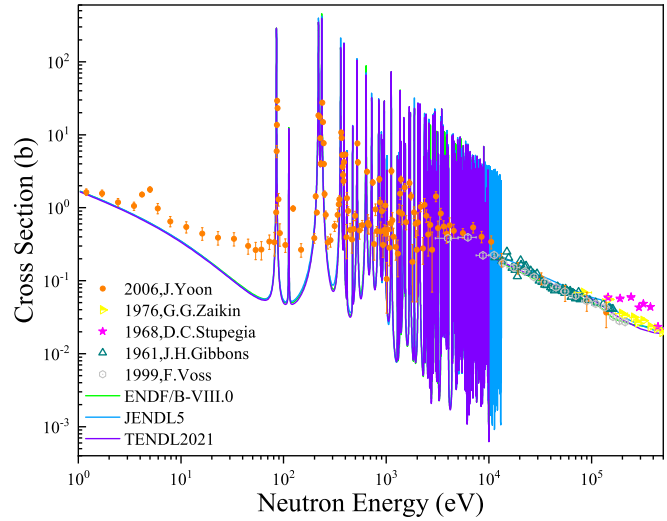


FIG. 2. The previous measurements of the $^{141}$Pr neutron capture cross section and the evaluated data.

0.00394 eV and 139 keV using the time-of-flight(TOF) method, unfortunately with insufficient precision for the resolved resonance region cross sections. In addition, the results of Stupegia *et al.* [8] in the range of 100–400 keV are significantly higher relative to other measurements. This measurement was made in the range of 1 eV to 500 keV, and in addition to giving more accurate results overall, some resonances that differed from the evaluated data as well as completely new resonances were found, and the details will be presented later.

The China Spallation Neutron Source (CSNS) is produced by bombarding a tantalum target with a pulsed proton beam with an energy of 1.6 GeV and a frequency of 25 Hz. The back streaming white neutron facility (Back-n), mainly used for neutron nuclear data measurements, is a branch line of the CSNS. It can provide a continuous neutron energy spectrum in the energy range of 0.1 eV to 400 MeV, and the neutron flux reaches $10^7$counts cm$^{-2}$ s$^{-1}$ [9–12]. This measurement was conducted in the double-beam mode, which uses two single-beam protons separated by 410 ns, to increase the beamline use efficiency. For each single-beam, the time structure is parabolic and the beam width is 60 ns. To achieve higher time resolution in detection, the experimental station ES#2, located further away (76 m) from the spallation target, was selected for this measurement. This approach also has the added benefit of reducing the background intensity of $\gamma$ rays within the neutron beam. Additionally, a Cd filter was placed at the beginning of the neutron beamline to absorb low-energy neutrons in the beam, preventing slow-moving neutrons from entering the subsequent pulsed beam and thereby reducing the precision of the time-of-flight (TOF) measurements. In the present work, the $(n, \gamma)$ cross section of $^{141}$Pr between 1 eV and 500 keV was measured to give precise results, and several resonances that differ from the evaluated data as well as suspected new resonances were also observed. The resonance parameters of $^{141}$Pr in the range of 1 eV to 2 keV were extracted and the Maxwellian-averaged cross section (MACS)

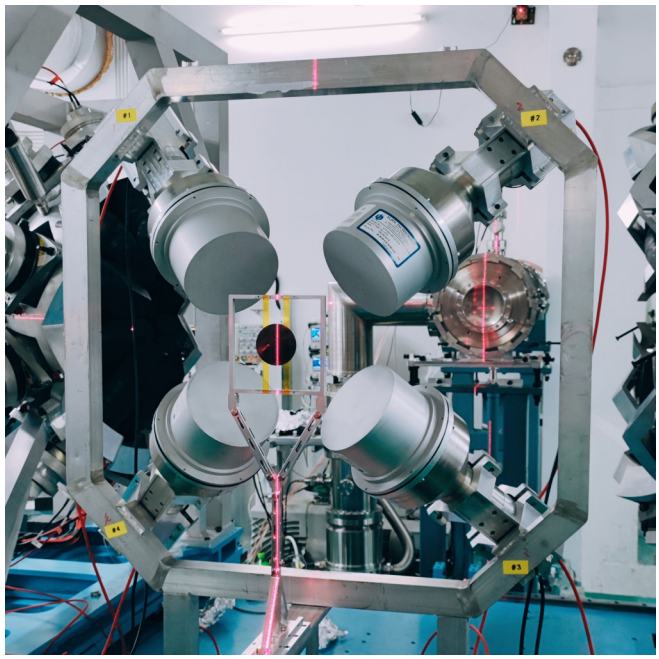

FIG. 3. Photo of the $C_6D_6$ detector system at Back-n. The position angle of the detector and the target holder relative to the neutron beam is the same as that of Ref. [12].

in the range of $kT = 5$ keV to $kT = 100$ keV were calculated based on our results. The experimental method and data processing procedures are as follows.

## II. EXPERIMENTAl METHOD

The hardware systems that this measurement relies on are mainly the $C_6D_6$ detector system and the data-acquisition system (see Fig. 3). The detector system consists of four $C_6D_6$ detectors, an aluminum detector holder and an aluminum sample holder. There are three reasons for choosing $C_6D_6$ to detect the prompt $\gamma$ ray emitted by the compound nucleus: (i) The $C_6D_6$ detector has relatively low neutron sensitivity. (ii) The detection efficiency of $C_6D_6$ detector can be made independent of the decay path of cascade $\gamma$ ray by a mathematical method named pulse-height weighting technique (PHWT) [13], which will be discussed in detail later. (iii) It has a relatively fast time response. Its core component, the liquid scintillator EJ315, has only ns response to neutron and gamma signals. In addition to the response time of the photomultiplier tube (PMT), the rise time of the entire anode signal is only about 10 ns. These signals are delivered into the readout electronics and converted into full waveform data with 1 GS/s sampling rate and 12-bit resolution [14]. The raw spectra of all targets were normalized using real-time recorded proton data for subsequent analysis. The neutron spectrum and proton number data were provided by Back-n [15,16] (see Fig. 3). And the neutron energy is obtained by the time-of-flight method, as follows:

$$E_n = \frac{1}{2}m_n v^2 = \left(\frac{72.2977L}{T}\right)^2, \tag{1}$$

TABLE I. Information of experiment targets.

| Material | Diameter (mm) | Thickness (mm) | Mass (g) | Purity |
|---|---|---|---|---|
| $^{141}$Pr | 40.0 | 2.000 | 17.57 | >99.9% |
| $^{nat}$C | 40.0 | 1.000 | 2.86 | >99.9% |
| $^{197}$Au | 40.0 | 0.198 | 4.83 | >99.99% |
| $^{nat}$Pb | 40.0 | 1.000 | 13.92 | >99.9% |

where the $L$ is the neutron flight length, $T$ is the neutron time of flight.

Four targets were used in this measurement, namely, $^{141}$Pr, $^{nat}$C, $^{nat}$Pb, and $^{197}$Au. The $^{nat}$C sample was used to subtract the scattered-neutron background, and $^{nat}$Pb was used to subtract the in-beam gamma background. $^{197}$Au was irradiated for 6 hours, and the data obtained were mainly used to correct the neutron flight distance $L$ and perform relative normalization on the capture cross section. In addition, analyzing the results of $^{197}$Au can also confirm whether the working state of the detection system is normal. The specific parameters of the target are shown in Table I.

## III. DATA ANALYSIS

In recent decades, the $C_6D_6$ detector system has gradually developed into a detection system commonly used in neutron capture cross-section measurements. In addition to its naturally low detection efficiency, the system needs to achieve another necessary condition: the detection efficiency of $\gamma$ rays is proportional to the $E_\gamma$. In practice, however, the detection efficiency of $C_6D_6$ usually does not increase linearly with $E_\gamma$, but varies nonlinearly with $E_\gamma$. Then the $\gamma$ ray detection efficiency will be determined by the specific deexcitation path, so that the accuracy of the measurement results cannot be guaranteed. Therefore, the introduction of the PHWT can satisfy the experimental requirement by calculating a detailed weighting function as shown in Eq. (2),

$$\varepsilon_\gamma = \alpha E_\gamma. \tag{2}$$

Based on this, the detection efficiency of the system for neutron capture events is proportional to the total excitation energy of the compound nucleus, independent of the deexcitation path. To achieve the relationship of Eq. (2), the weighting function is introduced, which is approximated as a polynomial function as Eq. (3),

$$W(E_i) = \sum_{k=0}^{4} a_k E_i^k, \tag{3}$$

where $E_i$ represents the energy response function of the $i_{th}$ bin, and $a_k$ is the parameter of the weighting function, which needs to be obtained by the least square method, such as Eq. (4),

$$\chi^2 = \sum_j \left[\alpha E_{\gamma j} - \int_{E_L}^{\infty} R(E_d, E_{\gamma j}) W(E_d) dE_d\right]^2, \tag{4}$$

where $E_L$ is the threshold of the PH spectrum and $R(E_d, E_{\gamma j})$ is the energy response of $C_6D_6$ to the $j_{th}$ $\gamma$ ray with energy $E_{\gamma j}$ [17], $E_d$ represents the energy deposited by the cascade

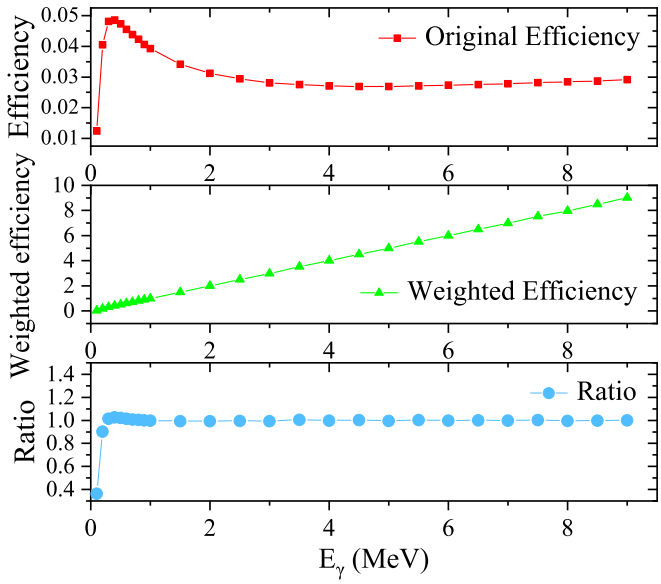


FIG. 4. (a) The $C_6D_6$ original efficiency. (b) Weighted efficiency. (c) The ratio of weighted efficiency to $\gamma$-ray energy.

$\gamma$ ray in the detector. Usually, $\alpha$ is set to 1. This allows the relationship of Eq. (2) to be achieved by weighting each capture event with a corresponding weighting function (WF). The weighted $C_6D_6$ detection efficiency is shown in Fig. 4, and its ratio to the $E_\gamma$ is approximated as 1.

The neutron capture yield can be obtained by Eq. (5),

$$Y_W(E) = \frac{N_w}{IS_n}, \tag{5}$$

where $N_w$ is the spectrum weighted and deducted from background, $I$ is the neutron intensity, and $S_n$ is the neutron binding energy. The neutron capture cross section can be calculated from the capture yield as follows:

$$\sigma_c(E) = \frac{Y_W(E)\sigma_t(E)}{(1 - e^{-N\sigma_t(E)tf_c})}, \tag{6}$$

where $t$ is the target thickness, $N$ is the atomic density, $\sigma_c$ is the $^{141}$Pr capture cross section, $\sigma_t$ is the $^{141}$Pr total cross section, and $f_c$ is the target thickness correction coefficient, it will be described later.

Evaluating and deducting background is a very important part of data analysis. The background components in this measurement are divided into two types: (1) The time-independent background $B_0$ mainly refers to the background brought by the environment and the sample itself. It is evaluated by measurements in the beamless state. (2) The time-dependent background; that is, the background related to the time structure of the neutron beamline [17]. Such backgrounds can only be evaluated experimentally in the beamed state. The second type of background can also be divided into target-related $B_{\text{sample}}(t_n)$ and target-independent backgrounds $B_{\text{empty}}(t_n)$. The target-independent background; that is, the environmental background in the beam-on state, refers to the background caused by the scattering of neutrons and $\gamma$ rays in the neutron beam into the ES#2 environment. After the beam is turned on, no sample is placed on the target holder in the beamline, and the data accumulated after a certain period of time is used to subtract this background. On the other hand, since the cross section of neutron scattering and $\gamma$-ray-induced interactions vary dramatically from nucleus to nucleus, part of the time-dependent background is also target-dependent. It is also the focus in background deduction. The total background $B_{\text{total}}$ can be expressed as

$$B_{\text{total}} = B_0 + B_{\text{empty}}(t_n) + B_{\text{sample}}(t_n), \tag{7}$$

where the $B_{\text{sample}}(t_n)$ consists of in-beam gamma background $B_{s\gamma}(t_n)$ and scattered-neutron background $B_{sn}(t_n)$, it can be expressed as

$$B_{\text{sample}}(t_n) = B_{sn}(t_n) + B_{s\gamma}(t_n). \tag{8}$$

The background induced by neutrons scattered from the sample $^{141}$Pr can be assessed with $^{\text{nat}}$C. A $^{\text{nat}}$C sample with a thickness of 1 mm and a diameter of 40 mm was placed in the beamline for irradiation. The residual spectrum of the respective samples (subtracting the environment background in the beam-on state), i.e., $N^C_{\text{residual}}$, was obtained, and the elastic-scattering yield ratio of $^{141}$Pr and $^{\text{nat}}$C corresponding to each neutron energy bin, i.e., $Q_{(\text{Pr,C})}$ was calculated [18]. The product of the yield ratio $Q_{(\text{Pr,C})}$ and the residual spectrum of the $^{\text{nat}}$C sample is the scattered-neutron background to be subtracted, as shown in Eq. (9),

$$B_{sn}(t_n) = N^C_{\text{residual}} Q_{(Pr,C)}. \tag{9}$$

$^{\text{nat}}$Pb has relatively high gamma scattering cross sections and low neutron-scattering cross sections, so it is used to evaluate the in-beam gamma background. One prerequisite is to first evaluate the scattered-neutron background due to $^{\text{nat}}$Pb itself. Again the scattered-neutron background is calculated using the yield ratio of $^{\text{nat}}$Pb and $^{\text{nat}}$C:

$$B_{s\gamma}(t_n) = \left(N^{\text{Pb}}_{\text{residual}} - Q_{(\text{Pb,C})} N^{\text{C}}_{\text{residual}}\right) K. \tag{10}$$

Equation (10) represents the final deducted in-beam gamma background, where $Q_{(\text{Pb,C})}$ represents the elastic-scattering yield ratio of $^{\text{nat}}$Pb and $^{\text{nat}}$C, and $K$ represents the normalization factor of the true in-beam gamma background. The $K$ coefficient was obtained using the black resonance filtering technique [19,20]. A 1.4-mm-thick $^{59}$Co and a 0.4-mm-thick $^{181}$Ta were placed upstream of the neutron beamline. The strong resonance structures of $^{59}$Co at 132.00 eV and 5.04 keV and $^{181}$Ta at 4.28 eV were used to absorb the vast majority of neutrons with that resonance energy. The normalization factor of the in-beam gamma background can be obtained by taking the valley resulting from the strong resonance as the true background level. Additionally, the TOF spectrum shows counts in the energy region where the neutrons should have been absorbed by Cd, which is thought to be due to sample activation. Therefore, the corresponding activation background is deducted in the acquisition of the residual spectrum of each target individually. The background components in this measurement are shown in Fig. 5.

Taking into account that the multiple-scattering effect of neutrons in the target may result in the actual travel path of particles in the target being larger than the target thickness, a target thickness correction factor $f_c$ was introduced.

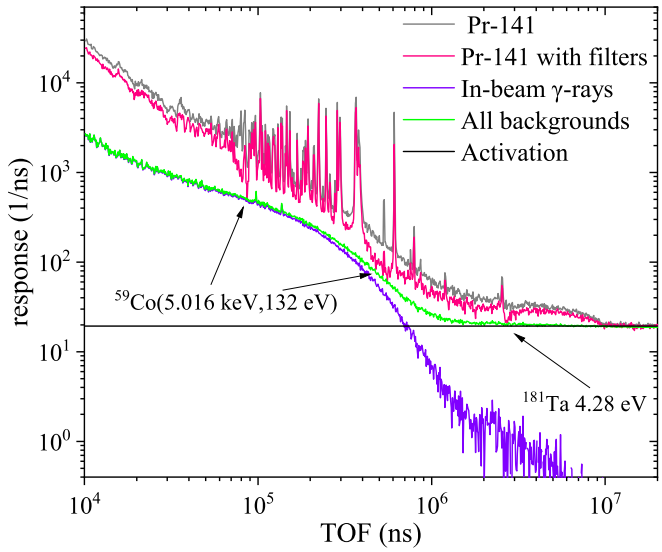


FIG. 5. Residual spectrum with and without filter (red and gray line). The in-beam gamma background (purple line) is normalized to the levels at the energy of several black resonances.

The sample was irradiated with a parallel neutron beam by the GEANT4 [21] code simulation, and the average length of the path traveled by neutrons with different energies in the target was calculated by counting the length of the path. The ratio of the average neutron transport length obtained from the simulation to the target thickness is the $f_c$ factor [22]. The $f_c$ factor as a function of neutron energy is plotted in Fig. 6.

Uncertainties mainly come from experimental conditions and data analysis. Among them, according to the analysis of Back-n neutron beam energy spectrum by Chen *et al.* [15], the uncertainty of energy spectrum is less than 8.0% below 0.15 MeV, and 2.3%–4.5% above 0.15 MeV. In addition, an uncertainty of about 1.5% in the CSNS proton beam flow was recorded during the experiment. Uncertainties in data analysis are mainly contributed by the PHWT method [23]. According

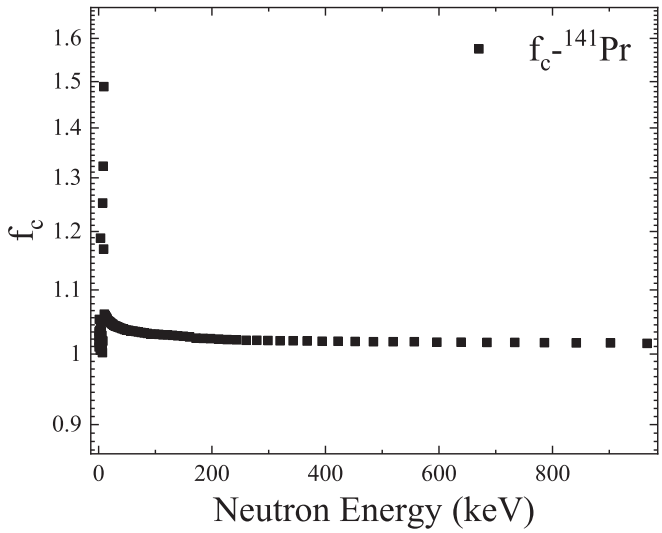


FIG. 6. The $f_c$ target thickness correction factor.

TABLE II. The statistic uncertainty and systematic uncertainty of this experiment.

| $\sigma$ | Uncertainty source | Value |
|---|---|---|
| | Experiment conditions | |
| $\sigma_{\phi 1}$ | Neutron energy spectrum below 0.15 MeV | <8.0% |
| $\sigma_{\phi 2}$ | Neutron energy spectrum above 0.15 MeV | <4.5% |
| $\sigma_{\text{Beam power}}$ | Proton beam power | <1.5% |
| | Data Analysis | |
| $\sigma_{\text{PHWT}}$ | Uncertainty from PHWT | <3.0% |
| | Statistical error | |
| $\sigma_{\text{Statistic}}$ | Statistic Uncertainty | <2.5% |

to the previous research by Tain *et al.* [24] on the systematic error of the PHWT method, the results are about 2.0% to 3.0%. The total uncertainty of the experimental results is less than 10.0%. The whole uncertainty is recorded in Table II.

## IV. RESULT AND DISCUSSION

### A. Resolved resonance region

For the resolved resonance region (RRR), neutron capture yields between 1 eV and 2 keV were analyzed using an *R*-matrix code [25] that takes into account all experimental effects such as multiple interaction events (multiple scattering), self-shielding, resonance broadening due to thermal motion and the resolution of the experimental setup. In this analysis we obtained resonance parameters such as resonance energy, $\gamma$ (width $\Gamma_\gamma$), neutron (width $\Gamma_n$), etc. The *R*-matrix fitting results are shown in Fig. 7. The initial parameters used in this fitting work are all taken from the TENDL-2021 [26] evaluated data library. And we used it to extract the capture kernel $k$, defined as

$$k = g\frac{\Gamma_n\Gamma_\gamma}{\Gamma_n+\Gamma_\gamma}, \tag{11}$$

where

$$g = \frac{2J+1}{(2s+1)(2I+1)}, \tag{12}$$

is the statistical factor $g$, which is given by the resonance spin $J$, the target spin $I$ and the neutron spin $s$.

The kernel $k$ of $^{141}$Pr obtained from the fitting are compared with those calculated from the TENDL-2021 data library, as shown in Fig. 8. The two fit well, and the specific data are shown in Table III.

The neutron capture yields obtained from the analysis of the experimental data were further converted to neutron capture cross sections for $^{141}$Pr within 1 eV to 500 keV, and the results are shown in Fig. 9. For the RRR, the measurement results are shown in Fig. 10. Based on the gradual improvement of measurement and data analysis methods in many experiments, this results have a high accuracy, and most of the resonance can be well consistent with the evaluated data. However, there are several differences.

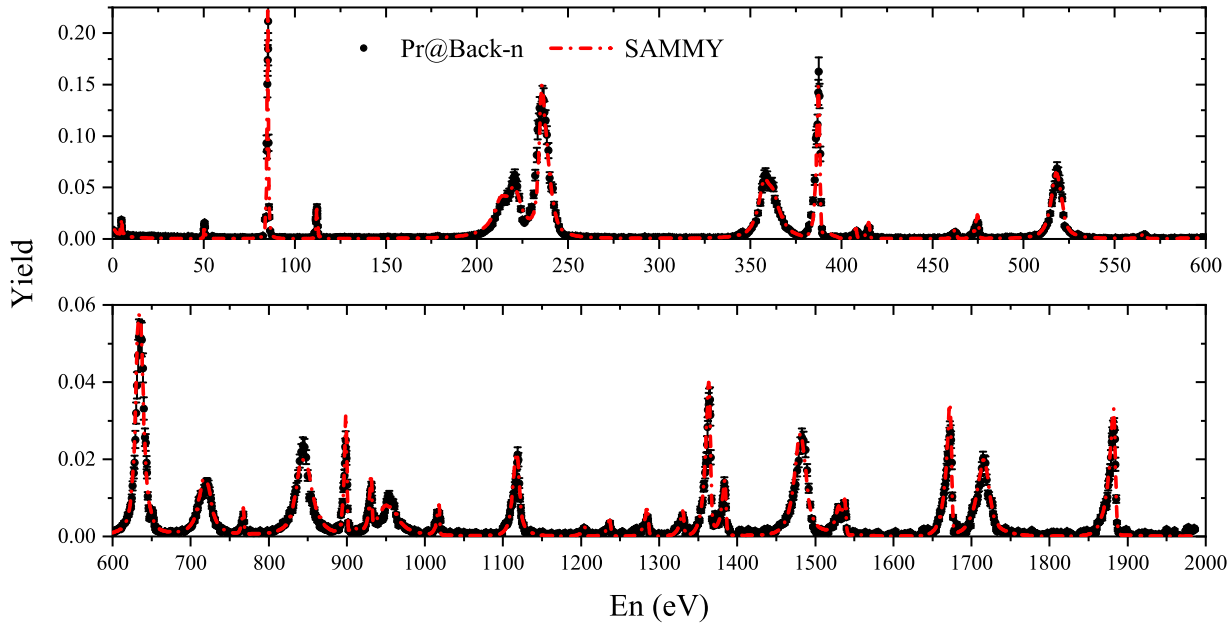


FIG. 7. Experimental capture yields fitted by *R*-matrix code.

In the RRR, due to the low density of the resonance energy level of $^{141}$Pr, some fluctuations caused by the influence of the neutron spectrum structure can be observed, such as many nonsmooth structures appearing before the 85 eV resonance. In addition, a resonance peak was observed at about 5.00 eV, which is consistent with the measurement results by Yoon *et al.* with the TOF method. The total cross-section measurement from Hickman [27] may support the present results. In contrast to result from Yoon *et al.*, a resonance peak at 50.43 eV was also clearly observed in this experiment, and we confirmed by analyzing the experimental original spectrum that this resonance peak was not produced by the influence of the neutron energy spectrum in the calculation. The neutron total cross section measurement from Vladimirski *et al.* [28] may support the present results. In addition, we obtained more accurate results than Yoon *et al.* between 1 and 2 keV, which could better match each resonance of the evaluated data libraries.

Notably, the evaluated data have two clear resonances at about 415 and 470 eV. But the present measurement observed resonance peak at about 408, 415, 462, and 474 eV. Out of concern for this being a result due to the influence of the double-beam mode, we used a so-called unfolding method [29] to deconvolute the two bunches in one pulse and found that the results remain unchanged at both locations. Therefore, these are considered as new findings. In addition, several resonance structures were found at the bottom of the valley, at about 703, 766, 1203, and 1236 eV. And they were fit in the *R*-Matrix fitting work as shown in Fig. 10.

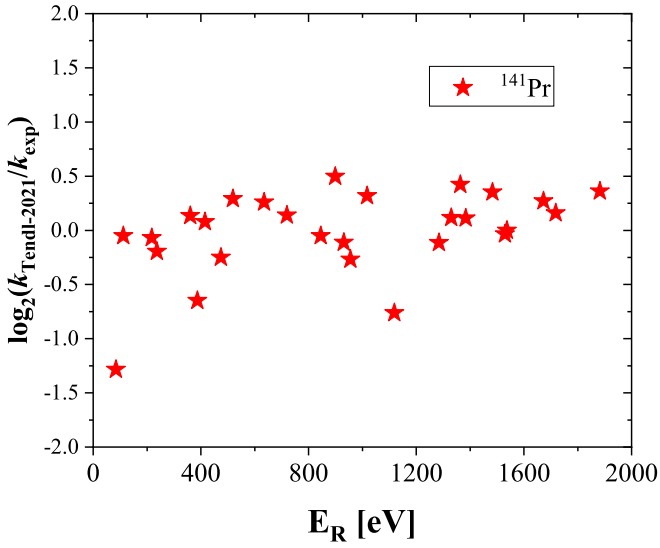


FIG. 8. The logarithm of ratio of kernel factor obtained from this result to TENDL-2021 evaluated data library.

TABLE III. Resonance energies $E_R$ and kernels $k$ up to 2 keV determined with *R*-matrix code.

| Mass | $E_R$ (eV) | $k$ meV | Mass | $E_R$ (eV) | $k$ (meV) |
|---|---|---|---|---|---|
| 141 | 85.14 | 0.86 | 141 | 955.89 | 33.14 |
| 141 | 112.15 | 0.18 | 141 | 1018.14 | 1.75 |
| 141 | 217.95 | 36.29 | 141 | 1118.51 | 27.26 |
| 141 | 236.9 | 34.32 | 141 | 1285.02 | 2.55 |
| 141 | 360.68 | 38.16 | 141 | 1330 | 2.96 |
| 141 | 387.67 | 9.34 | 141 | 1364.12 | 38.83 |
| 141 | 415.23 | 0.64 | 141 | 1384.34 | 5.66 |
| 141 | 474.96 | 1.29 | 141 | 1483 | 67.87 |
| 141 | 519.1 | 41.28 | 141 | 1529.73 | 3.63 |
| 141 | 634.8 | 58.62 | 141 | 1537.58 | 5.47 |
| 141 | 719.59 | 32.70 | 141 | 1672.69 | 26.66 |
| 141 | 845.7 | 45.20 | 141 | 1718.56 | 55.52 |
| 141 | 899.11 | 5.38 | 141 | 1880.7 | 35.40 |
| 141 | 931.3 | 2.60 | | | |

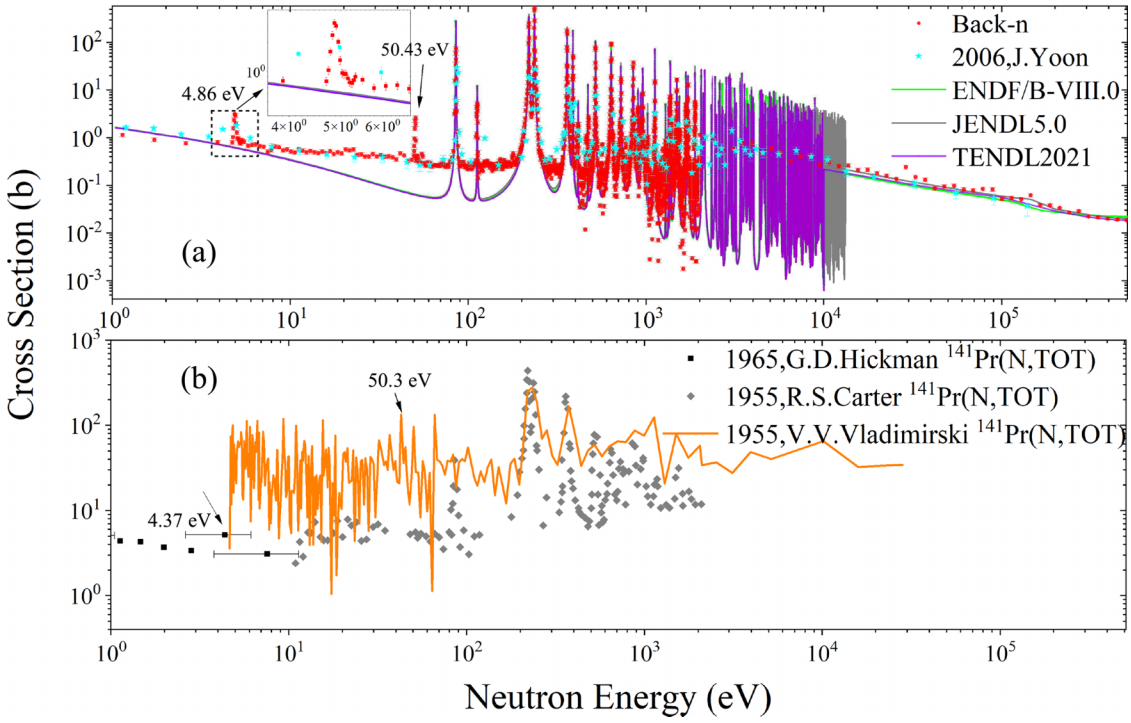


FIG. 9. (a) This measurement of $^{141}$Pr neutron capture cross section (red dots). (b) Previous measurements of $^{141}$Pr total neutron cross section.

### B. Unresolved resonance region

Since the neutron energy spectrum has a large impact on the results in unresolved resonance region (URR), the $^{141}$Pr capture cross section of URR (10–500 keV) needs to be given relative to the $^{197}$Au capture cross section results by the following equation,

$$\sigma_{Pr} = \frac{\langle \sigma_{\mathrm{Pr}} \rangle}{\langle \sigma_{\mathrm{Au}} \rangle} \sigma_{\mathrm{Au}}, \tag{13}$$

where $\langle \sigma_{Pr} \rangle$ is the neutron capture cross section of $^{141}$Pr, $\langle \sigma_{\mathrm{Au}} \rangle$ represents the experimental results of $^{197}$Au $(n, \gamma)$ cross

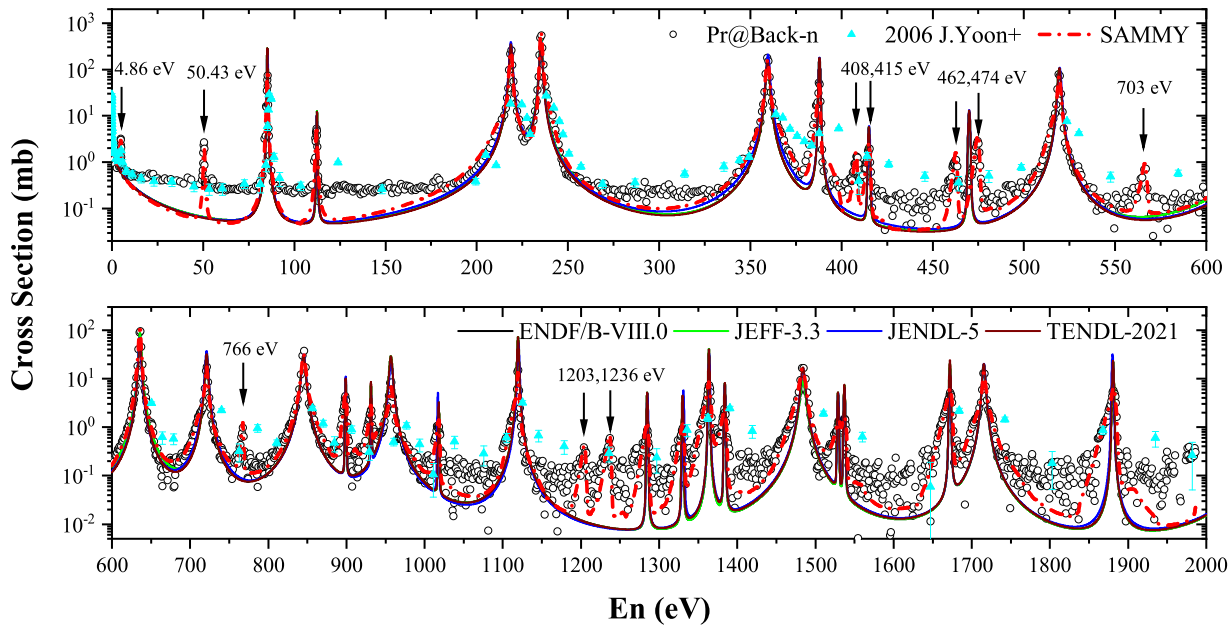


FIG. 10. The neutron capture cross section for $^{141}$Pr in the range of 1–2000 eV. The hollow circle symbols are the results of this work. The solid black, green, brown, and blue lines are $^{141}$Pr capture cross sections from evaluated data libraries. The red dotted line is the neutron capture cross section obtained from the calculation of SAMMY fitting results.

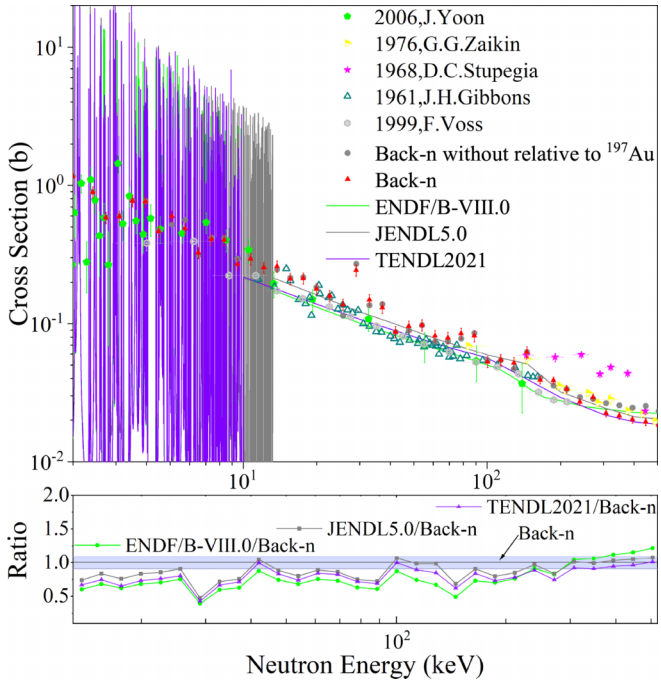


FIG. 11. The neutron capture cross section of $^{141}$Pr in the unresolved resonance region from 10 to 500 keV.

section, which are consistent with earlier data [30,31], and $\sigma_{\mathrm{Au}}$ is the evaluated data from JENDL-5.0 [32] evaluated library.

The results in the URR are shown in Fig. 11. It shows that Yoon's measurements are in good agreement within the error range and with the data from all three evaluated libraries. The results of Gibbons *et al.* [33] and Voss *et al.* [34] are generally closer to the evaluated data of ENDF/B-VIII.0 [35] and TENDL-2021. The results of Zaikin *et al.* [36] are more in line with the JENDL-5.0 evaluated data in the range of 80–350 keV and slightly higher than the other evaluated data. Finally, The results of Stupegia *et al.* are too high for any of the evaluated data. For this measurement, the overall data density is much higher than the Yoon's result. Before 90 keV, the cross section at some of the energy points is higher compared with the the results of Gibbons *et al.* and Voss *et al.* as well as to the evaluated data. For instance, the presence of a peak structure can be observed at about 29 keV, where the measurement is about 94.5% higher than the JENDL-5.0 evaluated data. This indicates that the results in URR are still influenced to some extent by the neutron energy spectrum. That can be seen in Fig. 11, where the results without relative to $^{197}$Au treatment are also shown. After 90 keV the present results are in general agreement with the evaluated data, and at some energy points the results are slightly lower than those of Zaikin *et al.* All results in the URR are presented in Table IV.

### C. Maxwellian-averaged cross section

For further applications of the $(n, \gamma)$ cross section in the study of *s* processes, the experimentally measured relevant data must be convolved with the neutron velocity distribution in the stellar plasma to obtain the Maxwellian-averaged cross section (MACS). The calculation of MACS requires a capture cross section over a sufficiently wide range of neutron energies, ideally from about 100 eV to 500 keV. This would be sufficient to cover the entire temperature range of the *s*-process scenario, including the highest temperatures reached during carbon shell burning in massive stars [50]. The experimental data were converted to MACS for $^{141}$Pr at

TABLE IV. The $(n, \gamma)$cross section and the uncertainties of $^{141}$Pr in the unresolved resonance region.

| $E_{\mathrm{low}}$ (keV) | $E_{\mathrm{high}}$ (keV) | $\sigma_{Pr}$ (barn) | Uncertainty (%) |
|---|---|---|---|
| 12.9 | 14.6 | 0.260 | 9.4 |
| 14.6 | 16.5 | 0.211 | 9.4 |
| 16.5 | 18.7 | 0.213 | 9.4 |
| 18.7 | 21.2 | 0.178 | 9.4 |
| 21.3 | 24.0 | 0.159 | 9.4 |
| 24.0 | 27.1 | 0.138 | 9.4 |
| 27.1 | 30.7 | 0.244 | 9.4 |
| 30.7 | 34.8 | 0.149 | 9.4 |
| 34.8 | 39.4 | 0.131 | 9.4 |
| 39.4 | 44.6 | 0.088 | 9.4 |
| 44.6 | 50.5 | 0.096 | 9.4 |
| 50.5 | 57.2 | 0.098 | 9.4 |
| 57.2 | 64.8 | 0.082 | 9.4 |
| 64.8 | 73.4 | 0.079 | 9.4 |
| 73.4 | 83.8 | 0.085 | 9.4 |
| 83.8 | 94.1 | 0.082 | 9.4 |
| 94.1 | 106.5 | 0.053 | 9.4 |
| 106.5 | 120.6 | 0.054 | 9.4 |
| 120.6 | 136.6 | 0.052 | 9.4 |
| 136.6 | 154.7 | 0.062 | 9.4 |
| 154.7 | 175.2 | 0.039 | 5.8 |
| 175.2 | 198.3 | 0.039 | 5.8 |
| 198.3 | 224.6 | 0.034 | 5.8 |
| 224.6 | 254.3 | 0.027 | 5.8 |
| 254.3 | 288.0 | 0.029 | 5.8 |
| 288.0 | 326.1 | 0.022 | 5.8 |
| 326.1 | 369.2 | 0.022 | 5.8 |
| 369.2 | 418.1 | 0.020 | 5.8 |
| 418.1 | 473.4 | 0.019 | 5.8 |
| 473.4 | 536.1 | 0.018 | 5.8 |

TABLE V. This experiment is compared with the MACS of KADoNiS about $^{141}$Pr at $kT$ = 5–100 keV.

| $kT$ | This work (mb) | KaDoNiS (mb) |
|---|---|---|
| 5 | 431.0 ± 42.15 | 412 |
| 10 | 293.3 ± 28.15 | 247 |
| 15 | 228.4 ± 21.75 | 182 |
| 20 | 189.7 ± 18 | 148 |
| 25 | 163.8 ± 15.5 | 126 |
| 30 | 145.0 ± 13.65 | 111.4 ± 1.4 |
| 40 | 119.3 ± 11.1 | 91.5 |
| 50 | 102.1 ± 9.35 | 78.3 |
| 60 | 89.5 ± 8.1 | 69.0 |
| 80 | 71.9 ± 6.25 | 56.2 |
| 100 | 59.7 ± 5.05 | 47.6 |

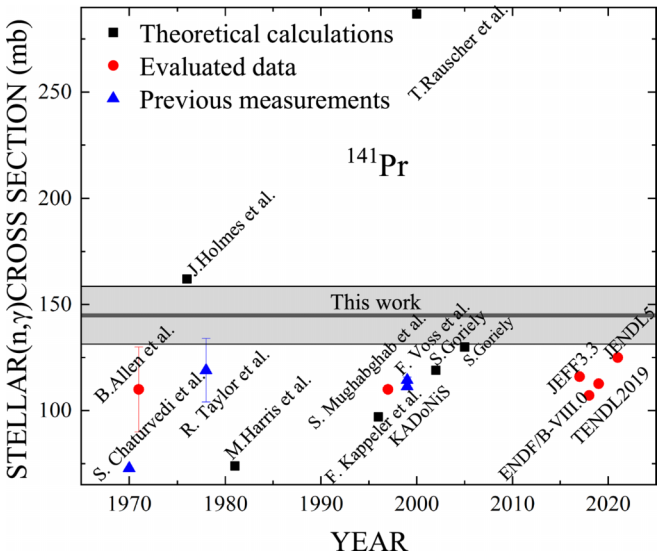


FIG. 12. The 30 keV $(n,\gamma)$ cross section of $^{141}$Pr (shaded band) compared with theoretical calculations (black squares), previous measurements (blue triangle), and evaluated data (red circles) [26,34,37–49].

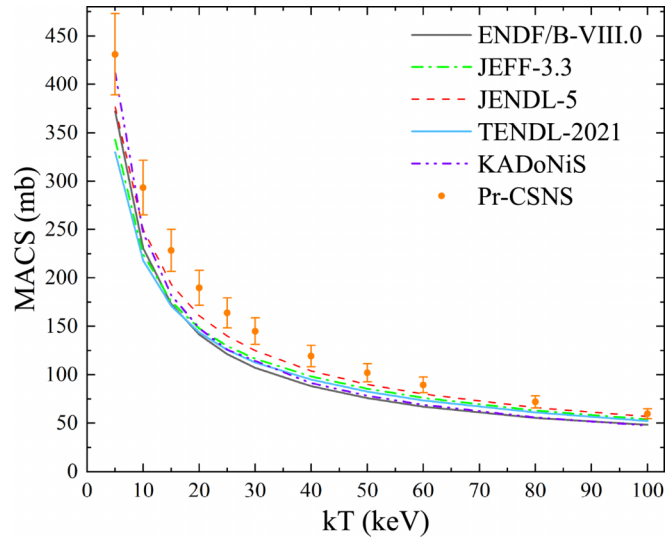


FIG. 13. Comparison of the experimental MACS from $kT$ = 5–100 keV with evaluated data.

$kT$ = 5–100 keV (see in Table V). And the results were compared with previous measurements (blue triangles), theoretical calculations (black squares), and evaluated data (red circles), as shown in Figs. 12 and 13. It is observed that this measurement is slightly high in most of the region of $kT$ = 5–100 keV, showing a trend of decreasing deviation with increasing energy.

## V. SUMMARY AND CONCLUSIONS

We measured the neutron capture cross section of $^{141}$Pr within 1 eV to 500 keV using the $C_6D_6$ detector system and the TOF method at the Back-n beam platform of CSNS. The experimental platform as well as the detector characteristics are briefly described, and the data analysis method is highlighted. It includes PHWT, background deduction method, etc. We obtained results with high accuracy in the resonance region, which can basically match with the evaluated data, and also observed some differences. The capture yields within 1eV to 2 keV were analyzed using the $R$-matrix code, and the resonance parameters were extracted. In the continuum region, the influence of the neutron energy spectrum leads to a partial bias in our results. Furthermore, accurate MACS were calculated in the temperature range of the $s$-process nucleosynthesis model.


[1] F. Käppeler *et al.*, Rep. Prog. Phys. **52**, 945 (1989).
[2] Cowan *et al.*, Phys. Rep. **208**, 267 (1991).
[3] F. Käppeler, R. Gallino, S. Bisterzo, and W. Aoki, Rev. Mod. Phys. **83**, 157 (2011).
[4] C. Freiburghaus *et al.*, Astrophys. J. **525**, L121 (1999).
[5] F. Käppeler, EPJ Web Conf. **63**, 03002 (2013).
[6] T. Wakabayashi, Spectr. **2**, 6 (1999).
[7] J. Yoon *et al.*, J. Nucl. Sci. Technol. (Abingdon, UK) **40**, 447 (2003).
[8] D. C. Stupegia *et al.*, J. Nucl. Energy **22**, 267 (1968).
[9] J. Y. Tang *et al.*, Nucl. Sci. Tech. **32**, 11 (2021).
[10] L. Y. Zhang *et al.*, Radiat. Phys. Chem. **127**, 133 (2016).
[11] Q. An *et al.*, J. Instrum. **12**, P07022 (2017).
[12] X. X. Li *et al.*, Phys. Rev. C **106**, 065804 (2022).
[13] R. L. Macklin and J. H. Gibbons, Phys. Rev. **159**, 1007 (1967).
[14] J. Ren *et al.*, Radiat. Detect. Technol. Methods **3**, 52 (2019).
[15] Y. H. Chen *et al.*, Eur. Phys. J. A **55**, 115 (2019).
[16] Q. Li *et al.*, Nucl. Instrum. Methods Phys. Res., Sect. A **946**, 162497 (2019).
[17] J. Ren *et al.*, Chin. Phys. C **46**, 044002 (2022).
[18] X. K. Li *et al.*, Eur. Phys. J. A **58**, 251 (2022).
[19] C. Lederer *et al.*, Phys. Rev. C **83**, 034608 (2011).
[20] D. B. Syme, Nucl. Instrum. Methods Phys. Res. **198**, 357 (1982).
[21] S. Agostinelli *et al.*, Nucl. Instrum. Methods Phys. Res., Sect. A **506**, 250 (2003).
[22] X. X. Li *et al.*, Chin. Phys. B **31**, 038204 (2022).
[23] X. X. Li *et al.*, Phys. Rev. C **104**, 054302 (2021).
[24] J. Tain *et al.*, J. Nucl. Sci. Technol. (Abingdon, UK) **39**, 689 (2002).
[25] N. M. Larson, Oak Ridge National Laboratory, Report No. ORNL/TM-2008/104, 2008.
[26] A. J. Koning *et al.*, Nucl. Data Sheets **155**, 1 (2019).
[27] G. D. Hickman, Bull. Am. Phys. Soc. **10**, 12 (1965).
[28] V. V. Vladimirski *et al.*, 1st UN Conf. Peaceful Uses Atomic Energy **4**, 22 (1955).
[29] H. Yi *et al.*, J. Instrum. **15**, P03026 (2020).
[30] X. X. Li *et al.*, Nucl. Tech. **43**, 80501 (2020).
[31] X. R. Hu *et al.*, Nucl. Sci. Tech. **32**, 101 (2021).
[32] O. Iwamoto *et al.*, EPJ Web Conf. **239**, 09002 (2020).

[33] J. H. Gibbons *et al.*, Phys. Rev. **122**, 182 (1961).
[34] F. Voss, K. Wisshak, C. Arlandini, F. Kappeler, L. Kazakov, and T. Rauscher, Phys. Rev. C **59**, 1154 (1999).
[35] D. Brown *et al.*, Nucl. Data Sheets **148**, 1 (2018).
[36] G. G. Zaikin *et al.*, Ukr. J. Phys. **16**, 1476 (1976).
[37] B. J. Allen *et al.*, Adv Phys. **4**, 205 (1971).
[38] M. B. Chadwick *et al.*, Nucl. Data Sheets **107**, 2931 (2006).
[39] T. Kawano *et al.*, J. Nucl. Sci. Technol. (Abingdon, UK) **39**, 108 (2002).
[40] T. Rauscher *et al.*, At. Data Nucl. Data Tables **75**, 1 (2000).
[41] F. Käppeler, K. A. Toukan, M. Schumann, and A. Mengoni, Phys. Rev. C **53**, 1397 (1996).
[42] M. J. Harris *et al.*, Astrophys. Space Sci. **77**, 357 (1981).
[43] J. Holmes *et al.*, At. Data Nucl. Data Tables **18**, 305 (1976).
[44] S. Goriely, Hauser-Feshbach rates for neutron capture reactions (2002).
[45] S. Goriely, Hauser-Feshbach rates for neutron capture reactions (2005).
[46] A. Santamarina *et al.*, JEFF Report **22**, 2 (2009).
[47] R. Taylor *et al.*, Aust. J. Phys. **32**, 551 (1979).
[48] S. Chaturvedi *et al.*, 13th Nucl. Phys. Solid State Phys. Symposy. **2**, 615 (1970).
[49] S. F. Mughabghab *et al.*, Neutron capture cross sections for nucleosynthesis (Brookhaven National Laboratory (BNL), Upton, NY (United States), 1997.
[50] G. Tagliente *et al.*, Phys. Rev. C, **84**, 015801 (2011).